








TDCOSMO

XVI. Measurement of the Hubble constant from the lensed quasar WGD 2038–4008

Kenneth C. Wong^{1,*}, Frédéric Dux^{2,3}, Anowar J. Shajib^{4,5,**}, Sherry H. Suyu^{6,7,8}, Martin Millon⁹, Pritom Mozumdar¹⁰, Patrick R. Wells¹⁰, Adriano Agnello¹¹, Simon Birrer¹², Elizabeth J. Buckley-Geer^{13,4}, Frédéric Courbin^{3,14,15}, Christopher D. Fassnacht¹⁰, Joshua Frieman^{4,5,13}, Aymeric Galan^{6,7}, Huan Lin¹³, Philip J. Marshall^{9,16}, Jason Poh^{4,5}, Stefan Schuldt^{17,18}, Dominique Sluse¹⁹, and Tommaso Treu²⁰

¹ Research Center for the Early Universe, Graduate School of Science, The University of Tokyo, 7-3-1 Hongo, Bunkyo-ku, Tokyo 113-0033, Japan

² European Southern Observatory, Alonso de Córdova 3107, Vitacura, Santiago, Chile

³ Institute of Physics, Laboratory of Astrophysics, Ecole Polytechnique Fédérale de Lausanne (EPFL), Observatoire de Sauverny, 1290 Versoix, Switzerland

⁴ Department of Astronomy & Astrophysics, University of Chicago, Chicago, IL 60637, USA

⁵ Kavli Institute for Cosmological Physics, University of Chicago, Chicago, IL 60637, USA

⁶ Technical University of Munich, TUM School of Natural Sciences, Physics Department, James-Franck-Straße 1, 85748 Garching, Germany

⁷ Max-Planck-Institut für Astrophysik, Karl-Schwarzschild-Str. 1, 85748 Garching, Germany

⁸ Academia Sinica Institute of Astronomy and Astrophysics (ASIAA), 11F of ASMAA, No. 1, Section 4, Roosevelt Road, Taipei 106216, Taiwan

⁹ Kavli Institute for Particle Astrophysics and Cosmology, Department of Physics, Stanford University, Stanford, CA, USA

¹⁰ Department of Physics and Astronomy, University of California, Davis, CA 95616, USA

¹¹ STFC Hartree Centre, Sci-Tech Daresbury, Keckwick Lane, Daresbury, Warrington WA4 4AD, UK

¹² Department of Physics and Astronomy, Stony Brook University, Stony Brook, NY 11794, USA

¹³ Fermi National Accelerator Laboratory, PO Box 500, Batavia, IL 60510, USA

¹⁴ ICC-UB Institut de Ciències del Cosmos, University of Barcelona, Martí Franquès, 1, E-08028 Barcelona, Spain

¹⁵ ICREA, Pg. Lluís Companys 23, Barcelona E-08010, Spain

¹⁶ SLAC National Accelerator Laboratory, Menlo Park, CA, USA

¹⁷ Dipartimento di Fisica, Università degli Studi di Milano, Via Celoria 16, I-20133 Milano, Italy

¹⁸ INAF – IASF Milano, Via A. Corti 12, I-20133 Milano, Italy

¹⁹ STAR Institute, Quartier Agora, Allée du Six Aout, 19c, B-400 Liège, Belgium

²⁰ Department of Physics and Astronomy, University of California, Los Angeles, 430 Portola Plaza, Los Angeles, CA 90095, USA

Received 4 June 2024 / Accepted 4 July 2024

ABSTRACT

Time-delay cosmography is a powerful technique to constrain cosmological parameters, particularly the Hubble constant (H_0). The TDCOSMO Collaboration is performing an ongoing analysis of lensed quasars to constrain cosmology using this method. In this work, we obtain constraints from the lensed quasar WGD 2038–4008 using new time-delay measurements and previous mass models by TDCOSMO. This is the first TDCOSMO lens to incorporate multiple lens modeling codes and the full time-delay covariance matrix into the cosmological inference. The models are fixed before the time delay is measured, and the analysis is performed blinded with respect to the cosmological parameters to prevent unconscious experimenter bias. We obtain $D_{\Delta t} = 1.68_{-0.38}^{+0.40}$ Gpc using two families of mass models, a power-law describing the total mass distribution, and a composite model of baryons and dark matter, although the composite model is disfavored due to kinematics constraints. In a flat Λ CDM cosmology, we constrain the Hubble constant to be $H_0 = 65_{-14}^{+23}$ km s⁻¹ Mpc⁻¹. The dominant source of uncertainty comes from the time delays, due to the low variability of the quasar. Future long-term monitoring, especially in the era of the *Vera C. Rubin* Observatory's Legacy Survey of Space and Time, could catch stronger quasar variability and further reduce the uncertainties. This system will be incorporated into an upcoming hierarchical analysis of the entire TDCOSMO sample, and improved time delays and spatially-resolved stellar kinematics could strengthen the constraints from this system in the future.

Key words. gravitational lensing; strong – cosmological parameters – distance scale

1. Introduction

The Hubble constant (H_0) is a key cosmological parameter that represents the present-day expansion rate of the Uni-

verse. Its value has important implications for the age, matter and energy content, and future of the Universe. In recent years, a discrepancy has emerged among various methods of constraining H_0 (see e.g., Verde et al. 2023, for a recent review). In particular, the results from the *Planck* mission find $H_0 = 67.4 \pm 0.5$ km s⁻¹ Mpc⁻¹ (Planck Collaboration VI

* Corresponding author; kcwong19@gmail.com

** NHFP Einstein fellow.

2020) in a flat Λ CDM cosmology based on observations of the cosmic microwave background (CMB). Other methods anchored in the early Universe find similar results (e.g., Macaulay et al. 2019; Schöneberg et al. 2022; Brieden et al. 2023; Madhavacheril et al. 2024). However, other measurements based in the local Universe tend to find a higher value (e.g., Freedman et al. 2019; Pesce et al. 2020; Anand et al. 2022; Palmese et al. 2024). The most precise constraint, from the Supernovae, H_0 , for the Equation of State of Dark Energy (SHOES) Collaboration, using type Ia supernovae calibrated by the Cepheid distance ladder, is $H_0 = 73.0 \pm 1.0 \text{ km s}^{-1} \text{ Mpc}^{-1}$ (Riess et al. 2022). These conflicting measurements may point to new physics beyond flat Λ CDM if they cannot be explained by systematic errors.

Strong gravitational lensing of variable sources, such as quasars or supernovae, can be used to constrain cosmological parameters through a technique known as “time-delay cosmography”. By measuring the time delay between multiple lensed images of the source, it is possible to constrain the “time-delay distance” to the lens system and thus H_0 (Refsdal 1964; Suyu et al. 2010). Typically, background quasars lensed by galaxies have been used for time-delay cosmography due to their brightness and variability on short timescales, along with the fact that galaxy-scale lenses are also more abundant on the sky and have a shorter time delay relative to cluster-scale lenses. Recent results using lensed supernovae (Kelly et al. 2023; Pascale et al. 2024) have shown promise, but such objects are still quite rare in comparison (see Suyu et al. 2024, and references therein).

The TDCOSMO Collaboration has been using time-delay cosmography to determine H_0 in a way that is independent of and complementary to other methods. The latest TDCOSMO results from a joint analysis of seven lensed quasars constrain H_0 to $\sim 2\%$ precision that is in agreement with late-Universe probes such as SHOES, assuming that the lens galaxies are accurately parameterized by a power-law or stars+dark matter mass profile (Millon et al. 2020a; Shajib et al. 2020; Wong et al. 2020). Relaxing this assumption gives an $\sim 8\%$ constraint (Birrer et al. 2020), which is statistically consistent with both *Planck* and SHOES. In order to use this technique to better constrain H_0 , more lensed quasars with inferred time-delay distances are needed to increase the sample size and reduce the current uncertainty.

In this paper, we present a measurement of the time-delay distance to the lensed quasar WGD 2038–4008 based on existing lens models (Shajib et al. 2022) and new time-delay measurements. To date, this is the only lens in the TDCOSMO sample that has been modeled by two independent teams using different modeling codes, which are combined into a final inference to account for systematic differences between the two. Since a time delay had not yet been measured when the models were developed in Shajib et al. (2022), they are effectively fixed prior to the measurement of the time delay, and we keep the cosmological parameter inference blinded until the analysis is completed to prevent any unconscious experimenter bias. The results were unblinded on May 14, 2024 after all primary authors consented, and the results were not subsequently modified in any way. The addition of this lens to the TDCOSMO sample will improve the overall constraint on cosmology.

This paper is organized as follows. We provide an overview of time-delay cosmography in Sect. 2. We describe the data we use in Sect. 3 and our procedure for the cosmographic inference in Sect. 4. We present our results in Sect. 5. We summarize our findings in Sect. 6. Throughout this paper, all magnitudes given

are in the AB system. All parameter constraints given are medians and 16th and 84th percentiles unless otherwise stated.

2. Time-delay cosmography

In this section, we summarize the principles behind time-delay cosmography, and refer the reader to, e.g., Treu et al. (2022), Treu & Shajib (2023), and Birrer et al. (2024) for recent comprehensive reviews. Light rays emitted from the background source experience a delay in arrival time at the observer because of the gravitational lensing effect. This time delay is the result of two physical effects: the excess path length of the deflected ray relative to the path it would take in the absence of lensing, and the time dilation arising from the ray passing through the gravitational potential of the lens (Refsdal 1964; Shapiro 1964). The excess time delay for a given lensed image (relative to an unlensed image) is

$$t(\boldsymbol{\theta}, \boldsymbol{\beta}) = \frac{D_{\Delta t}}{c} \phi(\boldsymbol{\theta}, \boldsymbol{\beta}), \quad (1)$$

where $\boldsymbol{\theta}$ is the image position, $\boldsymbol{\beta}$ is the source position, ϕ is the “Fermat potential” at the image position, c is the speed of light, and $D_{\Delta t}$ is the time-delay distance. The Fermat potential is defined as

$$\phi(\boldsymbol{\theta}, \boldsymbol{\beta}) \equiv \frac{(\boldsymbol{\theta} - \boldsymbol{\beta})^2}{2} - \psi(\boldsymbol{\theta}), \quad (2)$$

where ψ is the deflection potential (a scaled projection of the gravitational potential) that is related to the (scaled) deflection angle α by $\nabla\psi \equiv \alpha$. The time-delay distance is defined as

$$D_{\Delta t} \equiv (1 + z_d) \frac{D_d D_s}{D_{ds}}, \quad (3)$$

where z_d is the lens redshift, and D_d , D_s , and D_{ds} are the angular diameter distances from the observer to the lens, the observer to the source, and the lens to the source, respectively. Each of the angular diameter distances in Eq. (3) is inversely proportional to H_0 , therefore $D_{\Delta t} \propto H_0^{-1}$.

In order to constrain $D_{\Delta t}$ (and therefore, H_0) from a lensed quasar, one must measure the time delay between at least one pair of images, and constrain the Fermat potential at the position of the same images from an accurate mass model of the lens. In practice, the time delay is measured by monitoring the lens over a period of time and comparing the light curves of the multiple images to look for common features corresponding to the same brightness fluctuation at the source. The mass model of the lens is generally constrained from high-resolution imaging data, either from space telescopes or ground-based telescopes with adaptive optics (e.g., Chen et al. 2019).

A complicating factor is the mass-sheet degeneracy (MSD), a mathematical transform that can change the time delays by a multiplicative factor λ (along with a rescaling in the unobservable source position), while leaving other observables unchanged (e.g., Falco et al. 1985; Schneider & Sluse 2013). This is equivalent to having an infinite sheet of mass in the lens plane with constant surface density $\kappa \equiv 1 - \lambda$ (in units of the critical density for lensing), although it can arise from both an internal transformation of the lens mass profile (λ_{int}) and mass external to the lens ($\lambda_{\text{ext}} \equiv 1 - \kappa_{\text{ext}}$). This can, therefore, rescale the inferred $D_{\Delta t}$ and H_0 by the same factor λ if not accounted for.

The internal transformation, λ_{int} , can be incorporated into a particular parameterization of the lens mass profile that is maximally conservative with respect to the MSD (Birrer et al. 2020)

and can be more tightly constrained with resolved kinematics of the lens galaxy (e.g., [Shajib et al. 2023](#); [Yildirim et al. 2023](#)). Throughout this analysis, we assume $\lambda_{\text{int}} = 1$, similar to previous TDCOSMO analyses for individual systems (e.g., [Suyu et al. 2013](#); [Wong et al. 2017](#); [Rusu et al. 2020](#); [Shajib et al. 2020](#)). Instead, we consider two model families (see Sect. 3.1), which allows us to see if there are hints of $\lambda_{\text{int}} \neq 1$. A more general result allowing for the maximal degeneracy with respect to the MSD will be incorporated into a future joint TDCOSMO analysis with all of the analyzed lenses (TDCOSMO Collaboration, in preparation).

The external convergence, κ_{ext} , can be constrained through an analysis of the mass along the line-of-sight (LOS) to the lens. By characterizing the overdensity of the LOS (typically using cosmological simulations calibrated by relative galaxy number counts), it is possible to generate a distribution of κ_{ext} values that can be factored into the final constraint (e.g., [Greene et al. 2013](#); [Rusu et al. 2017](#); [Wells et al. 2023, 2024](#)).

3. Data

The quadruply-imaged lensed quasar WGD 2038–4008 was discovered in the Dark Energy Survey (DES) footprint by [Agnello et al. \(2018\)](#) through a combined search with the Wide-Field Infrared Survey Explorer (WISE) and the *Gaia* mission. The lens redshift is $z_d = 0.2283$, and the source redshift is $z_s = 0.777$ ([Buckley-Geer et al. 2020](#)). The uncertainties on z_d and z_s are small enough to have a negligible impact on the results, so we assume they are fixed throughout the analysis.

3.1. Fermat potential

WGD 2038–4008 was modeled using imaging data from the Wide-Field Camera 3 (WFC3) on the *Hubble* Space Telescope (HST). The data are taken in three filters: F475X and F814W in the ultraviolet-visual (UVIS) channel, and F160W in the infrared (IR) channel. Fig. 1 shows a composite color image of the lens system using these data ([Shajib et al. 2019](#)).

The lens was modeled by two independent teams in order to evaluate the consistency between two different lens modeling codes, GLEE ([Suyu & Halkola 2010](#); [Suyu et al. 2012](#)) and LENSTRONOMY ([Birrer & Amara 2018](#); [Birrer et al. 2021](#)). The details of the models are presented by [Shajib et al. \(2022\)](#), and we summarize them here. The two modeling teams each fit both an elliptical power-law total mass model and a stars+dark matter (hereafter, “composite”) mass model, including external shear. The models are constrained by the quasar image positions, as well as the surface brightness distribution of the lensed arcs from the quasar host galaxy in all three bands. At the time of the analysis, a time delay had not yet been measured for WGD 2038–4008, so the results were presented in terms of the Fermat potentials and time delays predicted by the models at the quasar image positions. We note that no modifications were made to the models from [Shajib et al. \(2022\)](#), so the Fermat potentials are effectively fixed before the measurement of the time delay.

Despite working independently without knowledge of the other team’s results, the power-law model results from both teams agreed to within $\sim 1\sigma$. However, both teams independently found structural problems with their composite models (an extremely low dark matter fraction for the GLEE team, and an unphysical velocity dispersion profile for the LENSTRONOMY team). The GLEE team made the decision to combine the power-law and composite model results with equal weight, while the

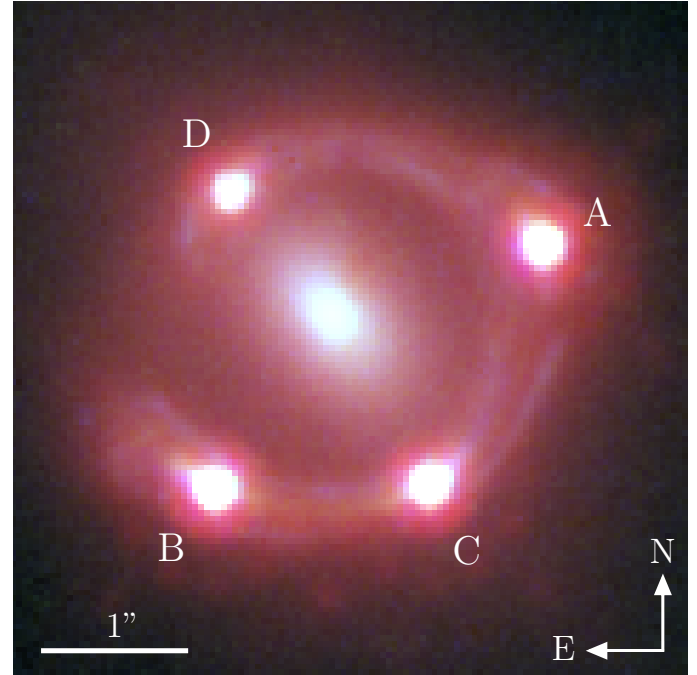


Fig. 1. HST RGB color-composite of the system WGD 2038–4008 combining the imaging data in the F160W, F814W, and F475X filters. The four images A, B, C, and D are labeled. The scale bar represents $1''$, and the arrows point to the north and east directions.

LENSTRONOMY team found that the predicted kinematics for their composite model were largely discrepant from the observed velocity dispersion, resulting in the power-law model receiving nearly all of the weight. Despite these different choices, the final constraints on the Fermat potentials were in good agreement (see [Shajib et al. 2022](#), Fig. 21).

3.2. Stellar velocity dispersion and line of sight effects

A measurement of the velocity dispersion of the lens, as well as an analysis of the environment to constrain the external convergence (κ_{ext}) based on relative galaxy number counts and the external shear from the lens model, is presented in [Buckley-Geer et al. \(2020\)](#). Both the kinematics and κ_{ext} were incorporated into the lens models to determine the final Fermat potentials ([Shajib et al. 2022](#)). As with the lens models, no modifications were made to the previously published results. Only a measurement of the time delay of WGD 2038–4008 is then needed to constrain $D_{\Delta t}$ using time-delay cosmography (Eq. 1).

The $D_{\Delta t}$ posterior without κ_{ext} and kinematics included will be used in an upcoming TDCOSMO hierarchical analysis (TDCOSMO Collaboration, in preparation), as those observables will be incorporated for treatment at the population level. For such future use cases, we present these results in Appendix A.

3.3. Time delay

WGD 2038–4008 was monitored in the *r*-band at two separate facilities, the Euler Swiss and ESO/MPG 2.2-m (2p2) telescopes, from April 2017 to October 2023. The general observing strategy adopted at the Euler telescope is detailed in [Courbin et al. \(2005\)](#) and [Eigenbrod et al. \(2005\)](#), and that of the 2p2 in [Courbin et al. \(2018\)](#) and [Bonvin et al. \(2019\)](#). Three seasons were accumu-

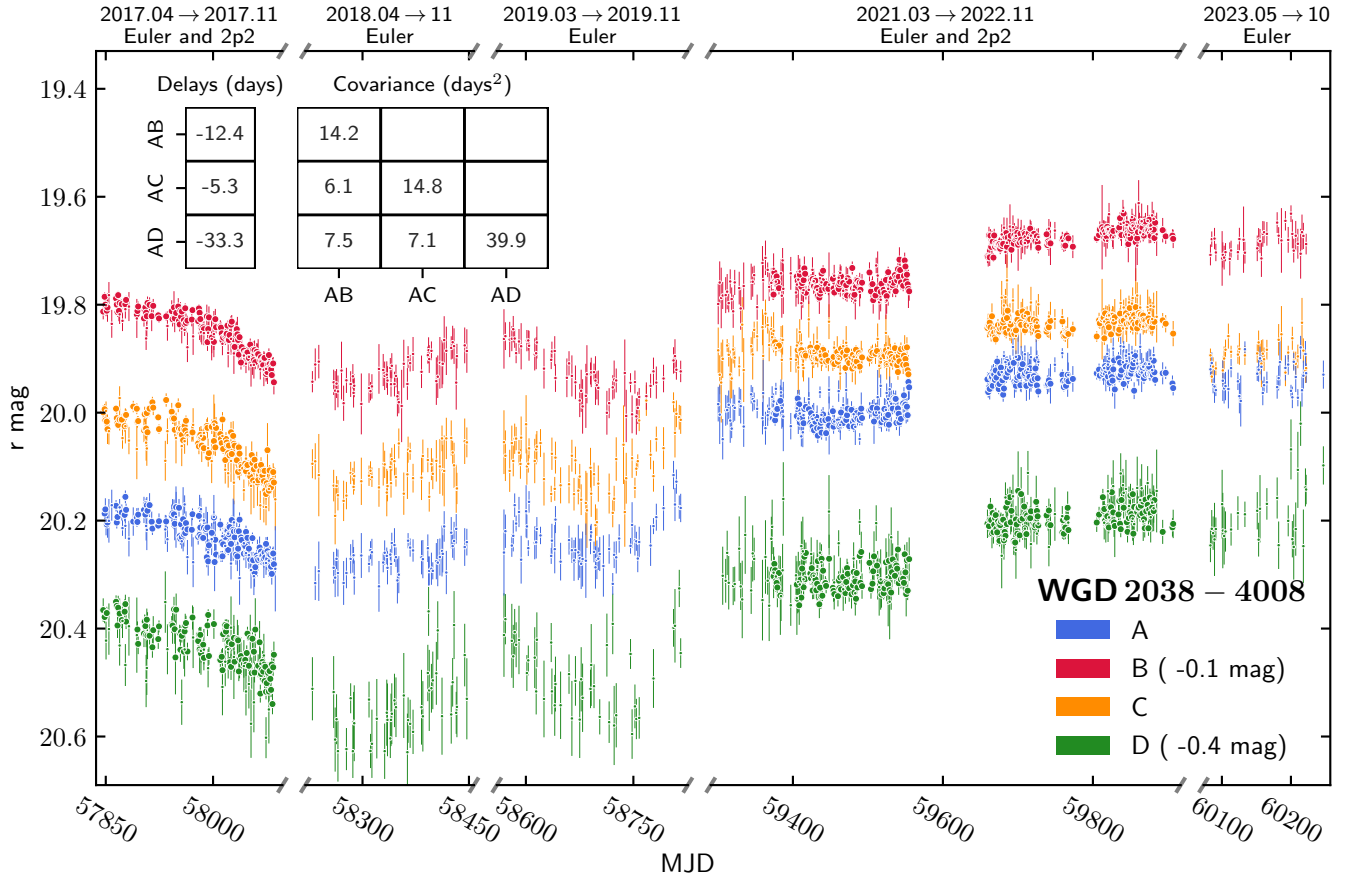


Fig. 2. *r*-band light curves of WGD 2038–4008, containing 3671 epochs of monitoring data. Data from the 2p2 and Euler telescopes are denoted by full disks and dots, respectively. When double coverage occurred, only the 2p2 data were used in the time-delay estimation. The median delays relative to image A, along with the corresponding covariance matrix, are shown in the upper left corner.

lated at daily cadence on the 2p2, with the first in 2017, the second in 2021 shortened by the COVID-19 pandemic, and the last in 2022 temporarily interrupted by a snowstorm that forced the closing down of the La Silla observatory. Concurrently, the Euler telescope captured five more seasons, cadenced at a point every two days. The photometric deblending, estimated time delays, and uncertainties for WGD 2038–4008 and other lensed quasars will be presented in an upcoming TDCOSMO paper (Dux et al., in preparation), but we summarize the strategy and findings regarding the present target here.

Despite the combined 3671 epochs of monitoring data plotted in Fig. 2, the WGD 2038–4008 quasar showed little variation, making delay measurements challenging. Nevertheless, comparing several initial guesses of the delay values from independent investigators showed an acceptable scatter, and their average was used as an initial starting point for value and uncertainty inference with the PyCS3 toolbox (Millon et al. 2020b). PyCS3 determines the values of the delays by optimizing the shifts between curves with different estimators and randomized initial shifts around the starting point. For uncertainties, it creates mock light curves with multiple realizations of the observed noise power spectrum, also adding artificial modulations to the individual curves, mimicking microlensing. The uncertainties are generally taken as the standard deviation of the resulting distributions of shifts. However, unlike previous H_0 estimations, where assuming uncorrelated errors in the delays was good enough to account for the uncertainty that maps into H_0 , the present case required accounting for significant covariance

among different delays. Therefore, the delays were weighted by their full 3×3 ¹ covariance matrix in the delay likelihood (as opposed to a diagonal covariance matrix). We provide the median time delays and covariance values with respect to image A, which we then use for the cosmographic inference (Sect. 4). Our notation of the A X delay, where X can be B, C or D, means $\Delta t_{AX} \equiv t_A - t_X$, where t is given in Eq. (1). The resulting delay and covariance values are given at the top left of Fig. 2.

We note that two possible time-delay solutions could fit the light curves equally well. In particular, the A C delay could either be negative (–5.3 days) or positive (+7.9 days), with only small repercussions on the values of the other delays. The change of sign between these two values is associated with a change in the order of arrival time between these two images. Both solutions were compared to the delays predicted by the mass models, and the solution with a negative A C delay was found to yield a much better χ^2 with respect to the model-predicted time delays. Because the ordering of the arrival time predicted by the lens model is very robust, we discarded the positive A C solution and estimated the delay covariance matrix around the negative A C solution only.

¹ There are 6 distinct delay pairs in a quadruply lensed quasar, but because PyCS3 shifts all available curves together, there are only 3 degrees of freedom. Hence the 6×6 covariance matrix combining all delay pairs is singular, while any 3×3 sub-matrix containing all delays relative to one given lensed image contains the full information.

Due to the faintness of the lensed images (Vega r -magnitudes between 20 and 21) and the relative lack of variability of the source quasar during the monitoring period, the observational constraints on the delays are weak. Neglecting covariance, we find a precision of 30%, 70%, and 20% on the A B, A C, and A D delays, respectively.

4. Cosmographic inference

We combine the Fermat potentials with the new time-delay measurements in order to place constraints on $D_{\Delta t}$. As discussed in Sect. 3.3, we use the delays relative to image A, along with the corresponding covariance matrix. The 3×3 matrix contains all of the time-delay information, which we verify by testing the delays relative to the other images with their corresponding covariance matrices and finding the differences to be negligible.

The observational data \mathcal{D} consists of the imaging data, kinematics, environment/LOS data, and time-delay measurements. The likelihood of the data can be expressed as

$$\begin{aligned} \mathcal{L}(\mathcal{D} | D_{\Delta t}) = & \int \mathcal{L}(\mathcal{D}_{\text{img,kin,LOS}} | \xi_{\text{model}}, \kappa_{\text{ext}}) \\ & \times \mathcal{L}(\mathcal{D}_{\text{td}} | \xi_{\text{model}}, \kappa_{\text{ext}}, D_{\Delta t}) \\ & \times p(\xi_{\text{model}}, \kappa_{\text{ext}}) d\xi_{\text{model}} d\kappa_{\text{ext}}. \end{aligned} \quad (4)$$

Here, ξ_{model} are the parameters of the lens model, including the lens and source light distributions. The probability density function $p(\xi_{\text{model}}, \kappa_{\text{ext}})$ is the prior on the model and external convergence parameters. In practice, the sampling of the posterior can be split into separate parts (e.g., the lens model, kinematics, LOS). All of the samplings aside from the time-delay likelihood were performed in Shajib et al. (2022), and we include the time-delay likelihood as the final piece of the inference in this work. We sample $D_{\Delta t}$ assuming a uniform prior in the range $0 \leq D_{\Delta t} \leq 4$ Gpc.

In addition to the constraint on $D_{\Delta t}$, which is independent of cosmology, we also constrain H_0 directly in a flat Λ CDM cosmology. We assume a uniform prior in the range $0 \leq H_0 \leq 150 \text{ km s}^{-1} \text{ Mpc}^{-1}$. We fix $\Omega_m = 0.3$ and $\Omega_\Lambda = 0.7$, as they are very weakly constrained by time-delay cosmography applied to a single system (e.g., Bonvin et al. 2017; Wong et al. 2020).

We first perform the inference for the GLEE and LENSTRONOMY models separately to evaluate the variation in the result due to the differences between lens modeling codes. For our final result, we need to combine the model constraints from GLEE and LENSTRONOMY. Statistically weighting the models from the two codes is complicated by the different choices made by each modeling team, including differences in the image reconstruction region and differences in the PSF reconstruction, among other things. Instead, we take the conservative approach of combining the model constraints from GLEE and LENSTRONOMY with equal weight to marginalize over any systematic differences between the two codes. This is the first TDCOSMO lens to incorporate multiple lens models into the final inference in this way.

The time-delay distance and the corresponding H_0 value are kept blinded until the time-delay measurement is finalized and all primary authors agree to unblind. This is done to prevent unconscious experimenter bias. We do this by either subtracting the median of the distributions or setting the median value to zero in any plots and tables viewed during the analysis. In this way, we are still able to view the spread of the distribution of these parameters and their covariances with other parameters, but not their absolute values until the analysis is finished. Once

the results were unblinded on May 14, 2024, no further modifications were made to any part of the analysis.

In principle, it is possible to constrain the angular diameter distance to the lens, D_d , by combining the lens model constraints with kinematics of the lens galaxy (e.g., Paraficz & Hjorth 2009; Jee et al. 2015, 2016), as has been done for some of the lenses in the TDCOSMO sample (Birrer et al. 2019; Chen et al. 2019; Jee et al. 2019). Since the models used in this work were already completed in Shajib et al. (2022), and incorporating D_d would require a new inference that would change the model weighting, we do not include D_d in order to maintain our blind analysis. The constraints from D_d tend to be weaker than those from $D_{\Delta t}$ when based on single aperture-averaged kinematic measurements of the lens galaxies (see e.g., Wong et al. 2020, Table 2), so they are unlikely to have a large impact on our results.

5. Results

In this section, we present the results of combining the new time delays with the Fermat potentials from Shajib et al. (2022), including the κ_{ext} and lens velocity dispersion from Buckley-Geer et al. (2020). As previously mentioned, the results without κ_{ext} and kinematics included are provided in Appendix A.

5.1. Time-delay distance

Using a uniform $D_{\Delta t}$ prior (Sect. 4), we first calculate the $D_{\Delta t}$ distributions for GLEE and LENSTRONOMY separately. In Fig. 3, we show the power-law model, composite model, and combined results for each of the two modeling codes. As described in Sect. 3.1 and Shajib et al. (2022), the combined results for GLEE give equal weight to the power-law and composite models, while the combined results for LENSTRONOMY give most of the weight to the power-law model based on kinematic constraints. The results for both modeling codes are in good agreement, and are presented in detail in Table 1.

Figure 4 shows the final joint constraint on $D_{\Delta t}$, weighting the combined GLEE and LENSTRONOMY models equally. We find $D_{\Delta t} = 1.68^{+0.40}_{-0.38}$ Gpc. This result is also presented in Table 1. The large uncertainty on this result is dominated by the time-delay measurement uncertainty, which ranges from 20–70% for the different image pairs resulting from the low variability of the source quasar. By comparison, the uncertainty on the Fermat potential differences between image pairs, including LOS and kinematics, ranges from just 7–13%.

5.2. H_0 in flat Λ CDM

Assuming a uniform prior on H_0 with fixed $\Omega_m = 0.3$ and $\Omega_\Lambda = 0.7$, we find $H_0 = 65^{+23}_{-14} \text{ km s}^{-1} \text{ Mpc}^{-1}$ in a flat Λ CDM cosmology. The final distribution, along with the individual GLEE and LENSTRONOMY constraints, is shown in Fig. 5, and the statistics for all distributions are presented in Table 2. As with the $D_{\Delta t}$ constraint, the uncertainty comes primarily from the time-delay measurement.

6. Summary

We present new time-delay measurements for the lensed quasar WGD 2038–4008. These delays are combined with the Fermat potentials from previously developed lens models to constrain the time-delay distance and Hubble constant in flat

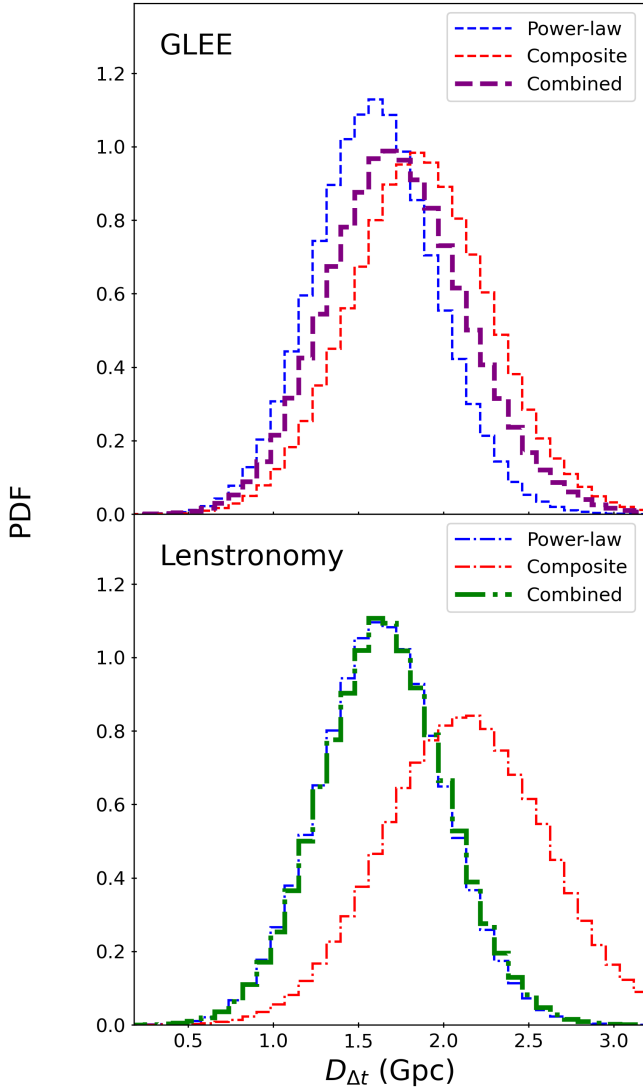


Fig. 3. $D_{\Delta t}$ distribution for GLEE (top) and LENSTRONOMY (bottom) for different mass models. The power-law (blue) and composite (red) model constraints are shown separately, as well as the combined constraint (purple and green, respectively) for each code. The GLEE results give equal weight to the power-law and composite models, while the LENSTRONOMY results give most of the weight to the power-law model based on the kinematics weighting. A flat prior in the range $0 \leq D_{\Delta t} \leq 4$ Gpc is assumed.

Λ CDM. The result combines models that assume either a power-law mass profile or a composite stars+dark matter profile, although the composite models were either down-weighted due to kinematics or showed unusual behavior in our previous analysis (Shajib et al. 2022). The analysis is performed blindly with respect to $D_{\Delta t}$ and H_0 . This is the first lens in the TDCOSMO sample to incorporate multiple lens models into the final result to account for systematic differences between lens modeling codes. It is also the first TDCOSMO lens to use the full time-delay covariance matrix in the cosmographic inference.

We determine the time-delay distance of WGD 2038–4008 to be $D_{\Delta t} = 1.68^{+0.40}_{-0.38}$ Gpc. We constrain the Hubble constant to be $H_0 = 65^{+23}_{-14}$ km s⁻¹ Mpc⁻¹ in flat Λ CDM, assuming $\Omega_m = 0.3$ and $\Omega_\Lambda = 0.7$. The dominant source of uncertainty in the cosmographic inference from this system comes from the time-

Table 1. Time-delay distance constraints.

Model	$D_{\Delta t}$ (Gpc)
GLEE power-law	$1.60^{+0.36}_{-0.35}$
GLEE composite	$1.86^{+0.41}_{-0.40}$
GLEE combined	$1.72^{+0.42}_{-0.39}$
LENSTRONOMY power-law	$1.64^{+0.37}_{-0.36}$
LENSTRONOMY composite	$2.13^{+0.48}_{-0.47}$
LENSTRONOMY combined	$1.65^{+0.37}_{-0.36}$
GLEE+LENSTRONOMY final	$1.68^{+0.40}_{-0.38}$

Notes. Reported values are medians, with errors corresponding to the 16th and 84th percentiles. A flat prior in the range $0 \leq D_{\Delta t} \leq 4$ Gpc is assumed.

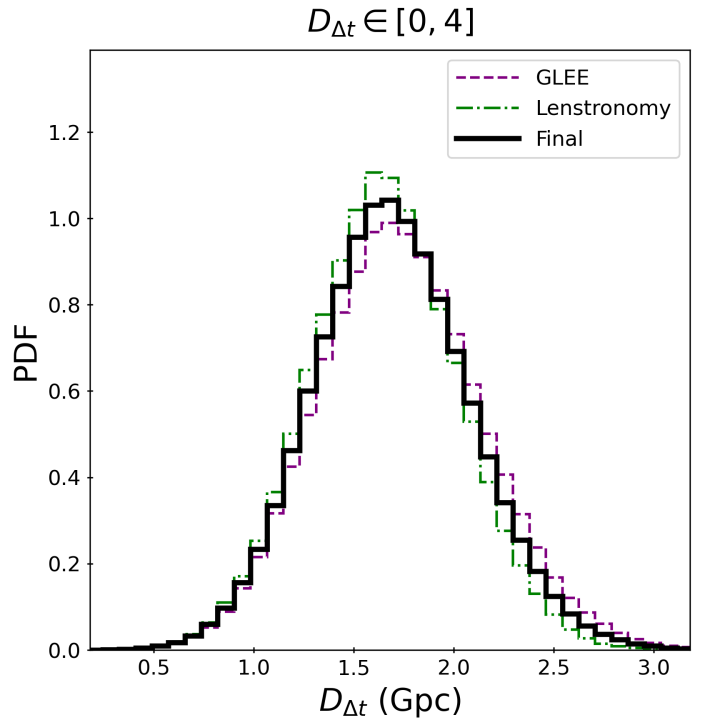


Fig. 4. $D_{\Delta t}$ distribution using a flat prior in the range $0 \leq D_{\Delta t} \leq 4$ Gpc. Shown are the results for GLEE (purple), LENSTRONOMY (green), and the final combined result (black).

delay measurements due to the low variability of the quasar. Future long-term monitoring, especially in the era of *Vera C. Rubin* Observatory’s Legacy Survey of Space and Time, could reduce the uncertainties by catching stronger quasar variability. Spatially-resolved kinematics of the lens galaxy could also improve the mass model constraints, particularly for the composite models.

Although the constraints from WGD 2038–4008 alone are too broad to shed light on the H_0 tension, it will be included as part of the full TDCOSMO sample in a future hierarchical analysis that will provide the most robust constraint on H_0 (in flat Λ CDM as well as other cosmologies) from time-delay cosmography to date (TDCOSMO Collaboration, in preparation).

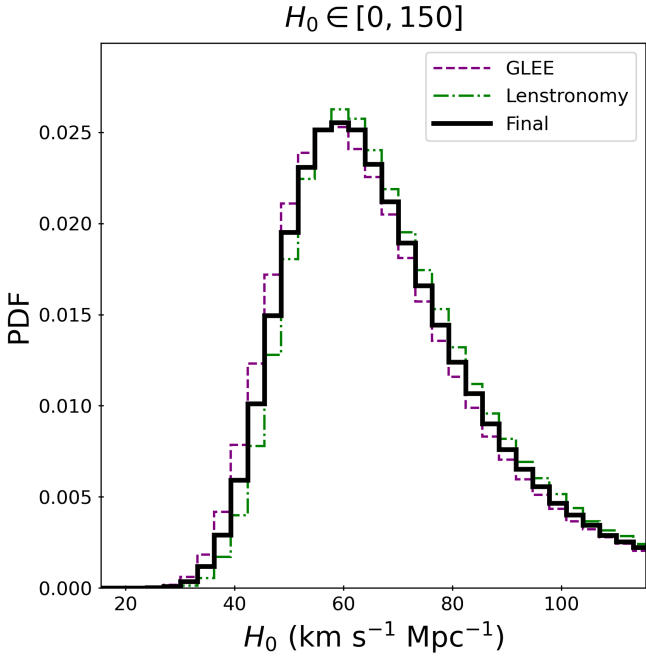


Fig. 5. H_0 distribution for flat Λ CDM using a flat prior in the range $0 \leq H_0 \leq 150 \text{ km s}^{-1} \text{ Mpc}^{-1}$. We assume $\Omega_m = 0.3$ and $\Omega_\Lambda = 0.7$. Shown are the results for GLEE (purple), LENSTRONOMY (green), and the final combined result (black).

Table 2. H_0 and $D_{\Delta t}$ constraints in a flat Λ CDM cosmology.

Model	H_0 ($\text{km s}^{-1} \text{ Mpc}^{-1}$)	$D_{\Delta t}$ (Gpc)
GLEE power-law	69^{+23}_{-14}	$1.43^{+0.36}_{-0.36}$
GLEE composite	59^{+21}_{-12}	$1.66^{+0.43}_{-0.43}$
GLEE combined	64^{+22}_{-14}	$1.53^{+0.43}_{-0.40}$
LENSTRONOMY power-law	67^{+23}_{-14}	$1.46^{+0.38}_{-0.37}$
LENSTRONOMY composite	52^{+18}_{-11}	$1.88^{+0.50}_{-0.49}$
LENSTRONOMY combined	67^{+23}_{-14}	$1.47^{+0.38}_{-0.38}$
GLEE+LENSTRONOMY final	65^{+23}_{-14}	$1.50^{+0.40}_{-0.39}$

Notes. Reported values are medians, with errors corresponding to the 16th and 84th percentiles. A flat prior in the range $0 \leq H_0 \leq 150 \text{ km s}^{-1} \text{ Mpc}^{-1}$ is assumed. We fix $\Omega_m = 0.3$ and $\Omega_\Lambda = 0.7$.

Acknowledgements. This work is supported by JSPS KAKENHI Grant Numbers JP20K14511, JP24K07089. This work received support from the Swiss National Science Foundation (SNSF) and by the European Research Council (ERC) under the European Unions Horizon 2020 research and innovation programme (COSMICLENS: grant agreement No. 787886). This work was supported by NASA through the NASA Hubble Fellowship grant HST-HF2-51492 awarded to AJS by the Space Telescope Science Institute, which is operated by the Association of Universities for Research in Astronomy, Inc., for NASA, under contract NAS5-26555. SHS thanks the Max Planck Society for support through the Max Planck Fellowship. This research is supported in part by the Excellence Cluster ORIGINS which is funded by the Deutsche Forschungsgemeinschaft (DFG, German Research Foundation) under Germany's Excellence Strategy – EXC-2094 – 390783311. MM acknowledges support by the SNSF (Swiss National Science Foundation) through mobility grant P500PT_203114. SS has received funding from the European Union's Horizon 2022 research and innovation programme under the Marie Skłodowska-Curie grant agreement No. 101105167 – FASTIDIoUS. This research is based in part on observations from the NASA/ESA Hubble Space Telescope program GO-15320, which is operated by the Space Telescope Science Institute. This research made use

of NUMPY (Oliphant 2015; Harris et al. 2020) and SCIPY (Jones et al. 2001; Virtanen et al. 2020). This research made use of MATPLOTLIB, a 2D graphics package used for PYTHON (Hunter 2007).

References

- Agnello, A., Lin, H., Kuropatkin, N., et al. 2018, *MNRAS*, 479, 4345
Anand, G. S., Tully, R. B., Rizzi, L., Riess, A. G., & Yuan, W. 2022, *ApJ*, 932, 15
Birrer, S., & Amara, A. 2018, *Phys. Dark Univ.*, 22, 189
Birrer, S., Treu, T., Rusu, C. E., et al. 2019, *MNRAS*, 484, 4726
Birrer, S., Shajib, A. J., Galan, A., et al. 2020, *A&A*, 643, A165
Birrer, S., Shajib, A., Gilman, D., et al. 2021, *J. Open Source Softw.*, 6, 3283
Birrer, S., Millon, M., Sluse, D., et al. 2024, *Space Sci. Rev.*, 220, 48
Bonvin, V., Courbin, F., Suyu, S. H., et al. 2017, *MNRAS*, 465, 4914
Bonvin, V., Millon, M., Chan, J. H. H., et al. 2019, *A&A*, 629, A97
Brieden, S., Gil-Marín, H., & Verde, L. 2023, *JCAP*, 2023, 023
Buckley-Geer, E. J., Lin, H., Rusu, C. E., et al. 2020, *MNRAS*, 498, 3241
Chen, G. C. F., Fassnacht, C. D., Suyu, S. H., et al. 2019, *MNRAS*, 490, 1743
Courbin, F., Eigenbrod, A., Vuissoz, C., Meylan, G., & Magain, P. 2005, in *Gravitational Lensing Impact on Cosmology*, eds. Y. Mellier, & G. Meylan, 225, 297
Courbin, F., Bonvin, V., Buckley-Geer, E., et al. 2018, *A&A*, 609, A71
Eigenbrod, A., Courbin, F., Vuissoz, C., et al. 2005, *A&A*, 436, 25
Falco, E. E., Gorenstein, M. V., & Shapiro, I. I. 1985, *ApJ*, 289, L1
Freedman, W. L., Madore, B. F., Hatt, D., et al. 2019, *ApJ*, 882, 34
Greene, Z. S., Suyu, S. H., Treu, T., et al. 2013, *ApJ*, 768, 39
Harris, C. R., Millman, K. J., van der Walt, S. J., et al. 2020, *Nature*, 585, 357
Hunter, J. D. 2007, *Comput. Sci. Eng.*, 9, 90
Jee, I., Komatsu, E., & Suyu, S. H. 2015, *JCAP*, 2015, 033
Jee, I., Komatsu, E., Suyu, S. H., & Huterer, D. 2016, *JCAP*, 2016, 031
Jee, I., Suyu, S. H., Komatsu, E., et al. 2019, *Science*, 365, 1134
Jones, E., Oliphant, T., Peterson, P., et al. 2001, *SciPy: Open Source Scientific Tools for Python*, <http://www.scipy.org>
Kelly, P. L., Rodney, S., Treu, T., et al. 2023, *Science*, 380, abh1322
Macaulay, E., Nichol, R. C., Bacon, D., et al. 2019, *MNRAS*, 486, 2184
Madhavacheril, M. S., Qu, F. J., Sherwin, B. D., et al. 2024, *ApJ*, 962, 113
Millon, M., Galan, A., Courbin, F., et al. 2020a, *A&A*, 639, A101
Millon, M., Tewes, M., Bonvin, V., Lengen, B., & Courbin, F. 2020b, *J. Open Source Softw.*, 5, 2654
Oliphant, T. E. 2015, *Guide to NumPy*, 2nd edn. (USA: CreateSpace Independent Publishing Platform)
Palmese, A., Kaur, R., Hajela, A., et al. 2024, *Phys. Rev. D*, 109, 063508
Paraficz, D., & Hjorth, J. 2009, *A&A*, 507, L49
Pascale, M., Frye, B. L., Pierel, J. D. R., et al. 2024, ArXiv e-prints [arXiv:2403.18902]
Pesce, D. W., Braatz, J. A., Reid, M. J., et al. 2020, *ApJ*, 891, L1
Planck Collaboration VI. 2020, *A&A*, 641, A6
Riess, S. 1964, *MNRAS*, 128, 307
Riess, A. G., Yuan, W., Macri, L. M., et al. 2022, *ApJ*, 934, L7
Rusu, C. E., Fassnacht, C. D., Sluse, D., et al. 2017, *MNRAS*, 467, 4220
Rusu, C. E., Wong, K. C., Bonvin, V., et al. 2020, *MNRAS*, 498, 1440
Schneider, P., & Sluse, D. 2013, *A&A*, 559, A37
Schöneberg, N., Verde, L., Gil-Marín, H., & Brieden, S. 2022, *JCAP*, 2022, 039
Shajib, A. J., Birrer, S., Treu, T., et al. 2019, *MNRAS*, 483, 5649
Shajib, A. J., Birrer, S., Treu, T., et al. 2020, *MNRAS*, 494, 6072
Shajib, A. J., Wong, K. C., Birrer, S., et al. 2022, *A&A*, 667, A123
Shajib, A. J., Mozumdar, P., Chen, G. C. F., et al. 2023, *A&A*, 673, A9
Shapiro, I. I. 1964, *Phys. Rev. Lett.*, 13, 789
Suyu, S. H., & Halkola, A. 2010, *A&A*, 524, A94
Suyu, S. H., Marshall, P. J., Auger, M. W., et al. 2010, *ApJ*, 711, 201
Suyu, S. H., Hensel, S. W., McKean, J. P., et al. 2012, *ApJ*, 750, 10
Suyu, S. H., Auger, M. W., Hilbert, S., et al. 2013, *ApJ*, 766, 70
Suyu, S. H., Goobar, A., Collett, T., More, A., & Vernardos, G. 2024, *Space Sci. Rev.*, 220, 13
Treu, T., & Shajib, A. J. 2023, ArXiv e-prints [arXiv:2307.05714]
Treu, T., Suyu, S. H., & Marshall, P. J. 2022, *A&ARv*, 30, 8
Verde, L., Schöneberg, N., & Gil-Marín, H. 2023, ArXiv e-prints [arXiv:2311.13305]
Virtanen, P., Gommers, R., Oliphant, T. E., et al. 2020, *Nat. Meth.*, 17, 261
Wells, P., Fassnacht, C. D., & Rusu, C. E. 2023, *A&A*, 676, A95
Wells, P. R., Fassnacht, C. D., Birrer, S., & Williams, D. 2024, *A&A*, 689, A87
Wong, K. C., Suyu, S. H., Auger, M. W., et al. 2017, *MNRAS*, 465, 4895
Wong, K. C., Suyu, S. H., Chen, G. C. F., et al. 2020, *MNRAS*, 498, 1420
Yıldırım, A., Suyu, S. H., Chen, G. C. F., & Komatsu, E. 2023, *A&A*, 675, A21

Appendix A: Results without κ_{ext} or kinematics

We present the results of the $D_{\Delta t}$ inference without including the external convergence (κ_{ext}) or stellar kinematics in Table A.1. We provide the constraints for the power-law and composite results, but not the combined constraints between the two, as removing the kinematics information changes the relative weighting of the models for LENSTRONOMY. These results will be included in an upcoming hierarchical analysis of the entire TDCOSMO sample (TDCOSMO Collaboration, in preparation), in which κ_{ext} and kinematics will be incorporated for treatment at the population level.

Table A.1. Time-delay distance constraints, without κ_{ext} or kinematics included.

Model	$D_{\Delta t}$ (Gpc)
GLEE power-law	$1.47^{+0.31}_{-0.32}$
GLEE composite	$1.64^{+0.35}_{-0.35}$
LENSTRONOMY power-law	$1.52^{+0.34}_{-0.33}$
LENSTRONOMY composite ^a	$1.86^{+0.41}_{-0.41}$
GLEE+LENSTRONOMY power-law	$1.49^{+0.32}_{-0.33}$
GLEE+LENSTRONOMY composite	$1.74^{+0.40}_{-0.39}$

Notes. Reported values are medians, with errors corresponding to the 16th and 84th percentiles. A flat prior in the range $0 \leq D_{\Delta t} \leq 4$ Gpc is assumed. ^aThe LENSTRONOMY composite model is highly excluded by the kinematics data if $\lambda_{\text{int}} = 1$ is assumed. Therefore, this value should not be used under this assumption. However, we provide this value for future usage with freely varying λ_{int} .